ELSEVIER

Contents lists available at ScienceDirect

Scripta Materialia

journal homepage: www.journals.elsevier.com/scripta-materialia





Micromechanical origin for the wide range of strength-ductility trade-off in metastable high entropy alloys $\!\!\!\!\!\!|^\dagger$

Zongyang Lyu^{a,#}, Zehao Li^{b,#}, Taisuke Sasaki^{b,*}, Yanfei Gao^{a,*}, Ke An^c, Yan Chen^c, Dunji Yu^c, Kazuhiro Hono^b, Peter K. Liaw^a

- ^a Department of Materials Science and Engineering, University of Tennessee, Knoxville, TN 37996, USA
- ^b National Institute for Materials Science, 1-2-1 Sengen, Tsukuba, 305-0047, Japan
- ^c Neutron Scattering Division, Oak Ridge National Laboratory, Oak Ridge, TN 37831, USA

ARTICLE INFO

Keywords: metastable high entropy alloy neutron diffraction transformation induced plasticity strength-ductility tradeoff microstructures

ABSTRACT

Through different annealing temperatures and times, it is reported here that interstitial metastable high entropy alloys (HEAs) can exhibit a wide range of strength-ductility trade-offs. The underlying mechanisms were investigated via in situ neutron diffraction, electron backscattered diffraction, and electron channel contrast imaging analyses. These techniques revealed that the phase transformation process could be tuned by various annealing processes, resulting in different degrees of load partitioning and sharing among different phases and grain families on the commensurate microstructural length scales. Therefore, the microstructures generated by thermal treatments and phase transformation from face-centered-cubic to hexagonal-close-packed phases could efficiently improve the ductility of the studied alloys.

Nowadays, with the demand for high-performance materials for industrial applications, many efforts have been made to seek alloys with both high strength and high ductility, but the strength-ductility trade-off unavoidably exists in most of such materials. High entropy alloys (HEAs), as a new alloying strategy in the last two decades, have opened up an extremely wide compositional space for alloy design with desirable mechanical properties [1-11]. Several different pathways have been explored in HEAs to break the strength-ductility trade-off, such as precipitations [5], gradient structures [6], hierarchical microstructures [7,12], phase transformations [8,12,13], interstitial solid solution [12, 13], and interstitial complexes [9]. An interstitial carbon-doped HEA with a hierarchical microstructure [12,13] has been developed recently which provides an efficient way to simultaneously improve strength and ductility by inducing transformation induced plasticity (TRIP) and twinning induced plasticity (TWIP) effects. The ductility could be improved from 14% to 60% by a multi-stage work hardening which is related to the sequential activation of TRIP and TWIP effects resulting

from the large variation in phase stability facilitated by hierarchical grains [12]. Excellent tensile property, i.e., 1.05 GPa of ultimate tensile strength and 35% of elongation, was achieved due to enhanced work face-centered-cubic hardening caused by (FCC) hexagonal-closed-packed (HCP) martensitic transformation in confined regions and twinning [13]. The deformation mechanisms of the interstitial HEA with hierarchical microstructures were discretely studied by electron backscatter diffraction (EBSD), transmission electron microscopy (TEM), and digital image correlation (DIC). However, the panorama of continuous deformation mechanism evolutions of the carbon-doped metastable HEA under loading is still not revealed because of the limitations of the post-mortem techniques and surface measurements. These experimental methods cannot quantitatively identify the load partitioning of different phases, as well as grain orientations, and hardly have the ability to track activations and changes of the deformation mechanisms. Thus, there is a large gap remaining in the understanding of consequences of dislocations, twins, new phases and

E-mail addresses: SASAKI.Taisuke@nims.go.jp (T. Sasaki), ygao7@utk.edu (Y. Gao).

[†] This manuscript has been co-authored by UT-Battelle, LLC, under contract DE-AC05-000R22725 with the US Department of Energy (DOE). The US government retains and the publisher, by accepting the article for publication, acknowledges that the US government retains a nonexclusive, paid-up, irrevocable, worldwide license to publish or reproduce the published form of this manuscript, or allow others to do so, for US government purposes. DOE will provide public access to these results of federally sponsored research in accordance with the DOE Public Access Plan (http://energy.gov/downloads/doe-public-access-plan).

[#] These two authors contribute equally to this paper.

^{*} Corresponding authors.

their interactions on the hardening behavior of these metastable HEAs.

In this work, a wide range of strength-ductility trade-offs was achieved in the interstitial metastable HEAs by different treatments without any changes of composition. Real-time in situ neutron diffraction and the EBSD and ECCI analyses were used to investigate the whole picture of the deformation mechanism evolution of the interstitial metastable HEAs under uniaxial tension, especially for the FCC to HCP martensitic transformation. Diffraction patterns could be acquired throughout the tensile tests, providing bulk averaged information over a certain gauge volume. The activation and evolution of TRIP and other lattice-level deformation mechanisms were determined and correlated with the work hardening behavior. The samples with different strength-ductility balance were found to have different characteristics for different grain orientations via the lattice strain evolutions. This work could fill the gap in the deformation mechanisms and systematically enrich the knowledge of the strength-ductility trade-off in interstitial TRIP HEAs with hierarchical microstructures by the conventional post-test/surface measurements and further promote the applications of HEAs.

A metastable Fe_{49.5}Mn₃₀Co₁₀Cr₁₀Co_{.5} alloy (at.%) [12] was prepared with pure elements (>99.9% wt.%) by vacuum induction melting and casting. The ingots were hot-rolled at 900°C with a 50% reduction in thickness and then homogenized at 1200 °C for 2 h followed by water-quenching. Finally, cold rolling was conducted with a 50% reduction in thickness. The plates were then machined to fabricate dog-bone shaped tensile test samples with the dimensions of $3\times2.6\times15$ mm in gauge section. Different heat treatments were used to form different microstructures, i.e., 650°C for 15 min, 700°C for 6 min, and 750°C for 30 s, 1 min, 2 min, 3 min followed by water-quenching, and they are designated as P650C-15m, P700C-6m, P750C-30s, P750C-1m, P750C-2m, and P750C-3m, respectively. We also prepared rod-shaped dog-bone samples with the dimensions of φ8×16 mm in gauge section. Three different heat treatment were conducted on the rod dog-bone samples, i.e., 650°C for 15 min, 700°C for 6 min, and 750°C for 3 min followed by water-quenching, and they are denoted as R650C-15m,

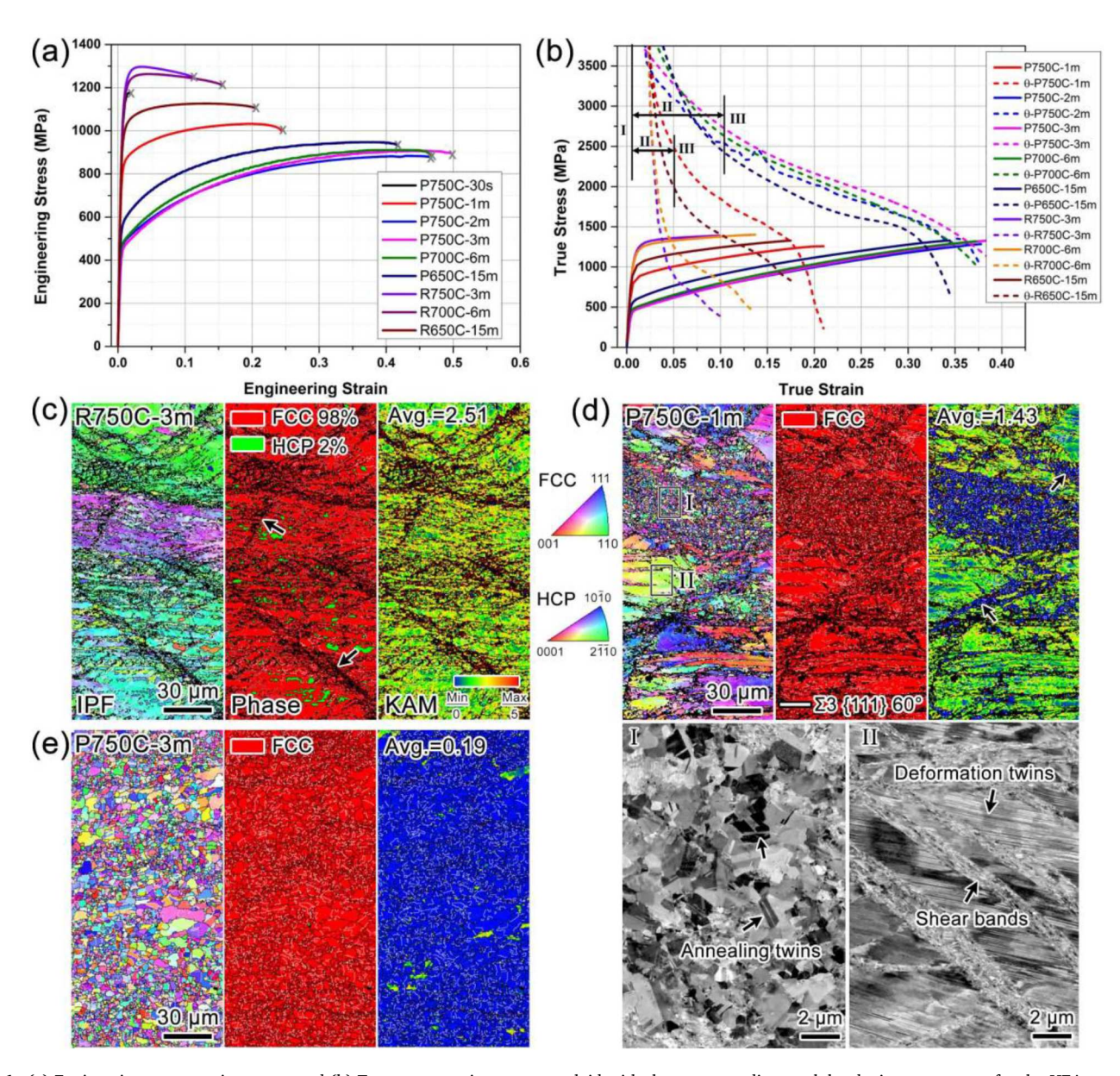


Fig. 1. (a) Engineering stress-strain curves, and (b) True stress-strain curves overlaid with the corresponding work-hardening-rate curves for the HEA samples in different processing conditions. Using the electron backscatter diffraction (EBSD) technique, here plotted are inverse pole figure (IPF), phase, and kernel average misorientation (KAM) maps of annealed (c) R750C-3m, (d) P750C-1m, and (e) P750C-3m samples. Enlarged electron channeling contrasting imaging (ECCI) results are taken from the rectangular regions I and II in (d).

R700C-6m, and R750C-3m, respectively. Microstructural analyses were performed using EBSD, Oxford Instruments HKL, in a Zeiss Crossbeam 1540 EsB scanning electron microscope (SEM) and electron channeling contrast imaging (ECCI) in a Zeiss Crossbeam 550 SEM operating at 20 kV. Samples for EBSD and ECCI analysis were mechanically ground followed by electropolished in an electrolyte of 10% perchloric acid and 90% ethanol at -20°C. In-situ neutron diffraction tests were performed under uniaxial tension, using an MTS load frame at the VULCAN Engineering Materials Diffractometer [14,15], the Spallation Neutron Source (SNS), Oak Ridge National Laboratory (ORNL). The in-situ neutron diffraction data were analyzed via the VULCAN Data Reduction and Interactive Visualization software (VDRIVE) [16]. The lattice strain of a specific (hkl) plane is determined by:

$$\varepsilon_{hkl} = \frac{d_{hkl} - d_{hkl}^0}{d_{hkl}^0} \tag{1}$$

where d_{hkl}^0 and d_{hkl} represent the lattice d-spacing in stress-free condition and the lattice d-spacing during loading condition, respectively.

Fig. 1(a) shows the engineering stress-strain curves of the samples. The rod samples of R750C-3m, R700C-6m, and R650C-15m show high yield strengths of $\sim\!1040, \sim\!1016,$ and $\sim\!900$ MPa, respectively, with low elongations of 11.3%, 15.5%, and 20.3%, respectively. In contrast, the plate samples heat treated under the same condition have lower strength and larger elongation than the rod samples; P750C-3m, P700C-6m, and P650C-15m samples have yield strength of $\sim\!400$ MPa, $\sim\!450$ MPa, and $\sim\!500$ MPa, respectively with the elongation of 49.8%, 46.5%, and 41.7%, respectively. The yield strength of the plates increased with decreasing the annealing time. P750C-30s, P750C-1m, and P750C-2m samples have yield strengths of 989, 794, and 450 MPa, respectively

with elongation of 1.6%, 24.4%, and 46.5%, respectively. After yielding, all the samples show a continuous hardening with a gradually decreasing strain hardening rate of Θ ($\Theta = d\sigma_{true}/d\varepsilon_{true}$ where σ_{true} is the true stress and ε_{true} is the true strain) during uniaxial tension, Fig. 1(b). Θ decreases almost linearly for the R750C-3m and R700C-6m rods until necking, and these rods took the area of low strain hardening rates. The P750C-1m and R650C-15m have the medium strain hardening rate part, while P750C-2m, P750C-3m, P700C-6m, and P650C-15m located in the zone of high strain hardening rates, Fig. 1(b). Multi-stage work hardening behavior, which is determined based on the micromechanical behaviors measured by in situ neutron diffraction, is observed for most of the samples other than R750C-3m and R700C-6m. Stage I could be a quick drop of work hardening rate which is usually related to the dislocation rearrangement [17]. In stage II, the work hardening rates continue to decline with gradually lower slope compared to stage I. The delineation between stages II and III is due to the commencement of phase transformation, as will be made clearly in Fig. 2. However, there is an obvious increase followed by a decrease of strain hardening rate in the P750C-2m sample during the strain stage of \sim 12.9% to 15.6%. Fig. 1 (c) shows the EBSD inverse pole figure (IPF), phase, and kernel average misorientation (KAM) maps obtained from the R750-3m sample. The IPF map shows many shear bands in black color penetrating through the flattened parent grains, indicating the retention of the deformed structure. The phase map shows that the microstructure consists mainly of FCC phase with a small amount of HCP phase, and the KAM map shows a high density of dislocations with a high average misorientation value of \sim 2.51. These features account for the high yield strength but low strain hardening rate of the R750-3m. In contrast, the plates show progressive recrystallization during annealing. The P750-1m, with moderate

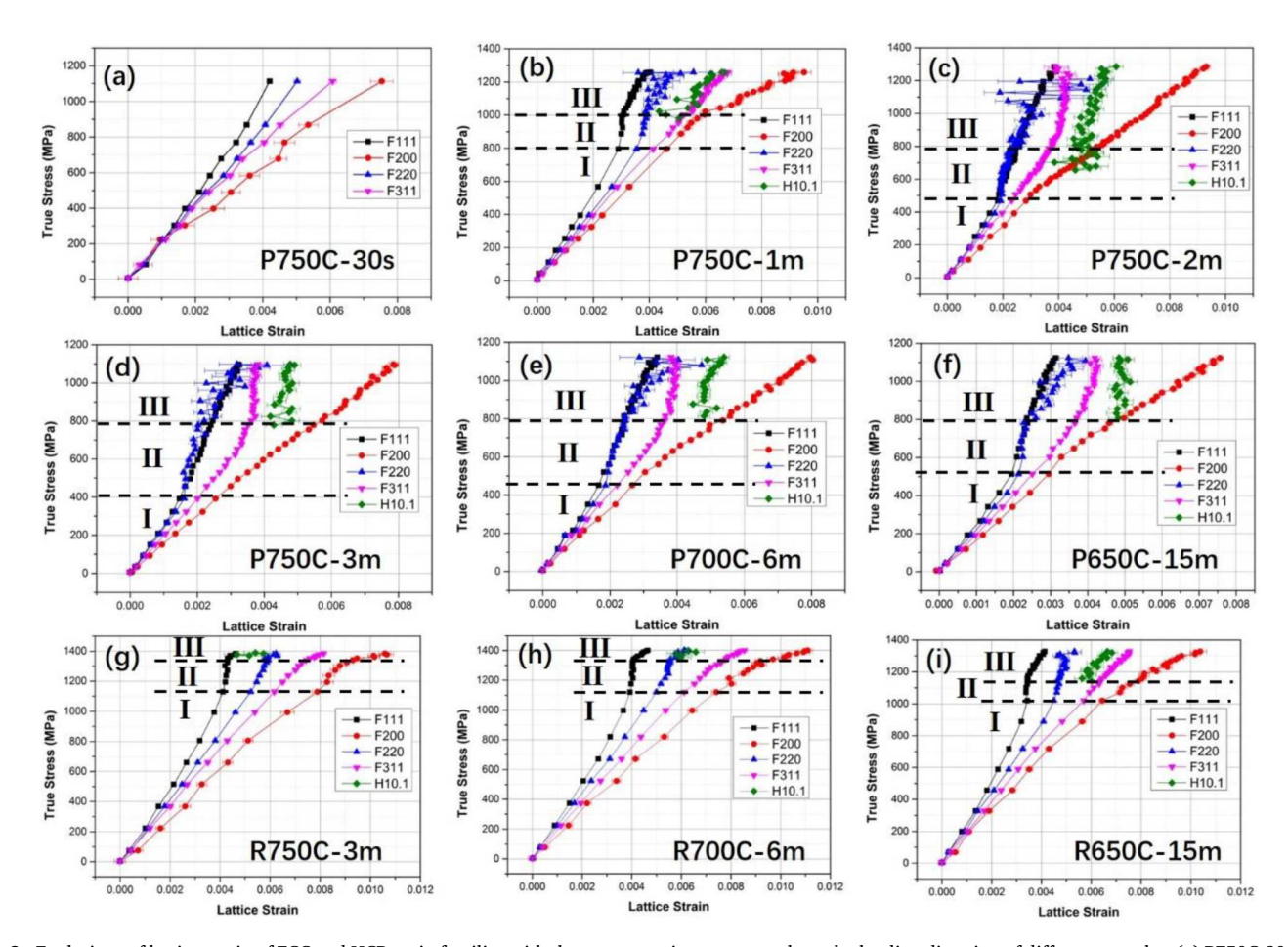


Fig. 2. Evolutions of lattice strain of FCC and HCP grain families with the macroscopic true stress along the loading direction of different samples: (a) P750C-30s, (b) P750C-1m, (c) P750C-2m, (d) P750C-3m, (e) P700C-6m, (f) P650C-15m, (g) R750C-3m, (h) R700C-6m, (i) R650C-15m.

Z. Lyu et al. Scripta Materialia 231 (2023) 115439

strength and strain hardening rate, exhibits a partially recrystallized structure and consists of a single FCC phase, as shown in the IPF and phase maps, Fig. 1(d). The KAM map reveals the nucleation of dislocation-free recrystallized grains with an average diameter of $\sim 1.2~\mu m$ in blue color near shear bands as indicated by arrows. Enlarged ECC images from the IPF map show the formation of annealing twins in the recrystallized grains (ROI-I), while dense deformation twins and shear bands remain in the parent grains (ROI-II). After the 3 min annealing, a nearly fully recrystallized structure (average grain size of $\sim 1.9~\mu m)$ with profuse annealing twins is obtained, which explains the further decrease in yield strength and the high strain hardening rate in the P750-3m sample.

Fig. 2 presents the lattice strain evolutions by in situ neutron diffraction under uniaxial tension. The load partitioning among different grain families can be differentiated with the lattice strain evolutions, which indicate the average stress of the corresponding grain families along the loading direction. All the grain families of different samples along the loading direction deform elastically with a linear relationship at stage I. After the linear part, the lattice strain of the {220} grain family had the first obvious upward trend at stage II for all plate samples except for the P750C-30s, which had almost no plastic deformation, Fig. 2(b-f). These transition points of the {220} grain family are identical to the yield points of the corresponding samples. For the rods in Fig. 2 (g-i), the first obvious upturns in lattice strain occurred in the {111} grain family, which are consistent with the yield stresses of the samples. This indicates that the {220} and {111} grain families play more important roles in the yielding process than other grain families in the plates and rods, respectively. The {200} grain family along the loading direction tends to share the largest load during deformation than other grain families in all the studied samples. For the P750C-2m, P750C-3m, P700C-6m, and P650C-15m in Fig. 2(c-f), they had low strength and high ductility, as well as high strain hardening rate, and tended to have an early FCC to HCP transformation at the stress of \sim 800 MPa. As a result of this early HCP martensite formation, the HCP phase started to share the load from FCC phase, and then the lattice strain of the {311} grain family bends up while the {200} grain family almost keep its original trend in stage III. The samples with medium strength-ductility-hardening rate, i.e., P750C-1m and R650C-15m, tend to have later phase transformation at 1000-1200 MPa as shown in Fig. 2(b) and 2(i). In this case, the HCP martensite may not change the intergranular strain much in the FCC phase. Therefore, the {311} lattice strain maintained a linear trend, and the {200} lattice strain was bent to the right, indicating more load shared by the {200} grain family. For the samples with higher strength, low ductility, and low work hardening rate, such as R750C-3m and R700C-6m, the HCP formed very late at the stress of ~1350 MPa, as shown in Fig. 2(g) and 2(h). The HCP martensite did not share load from the FCC phase before the lattice strain of the {311} grain orientation started to bend to the right.

Fig. 3(a) and 3(b) show the FCC fraction evolutions and true stressstrain curves for P750C-1m and P750C-3m, respectively. Since FCC to HCP transformation is closely related to stress [18], the stresses required to form FCC decreases to $\sim\!953$ MPa and $\sim\!750$ MPa for P750C-1m and P750C-3m, respectively, indicating the ease of activation of phase transformation in P750C-3m than P750C-1m. This could be related to the stacking fault energy (SFE) [19,20] and grain size [21]. The nucleation and growth of HCP phase are mainly accompanied by the overlapping of stacking faults controlled by the movement of Shockley partial dislocations [22]. The decrease of FCC fraction was suppressed after the true strain reached ~20%, which could be related to higher activation stresses to nucleate the transformation in the ultrafine recrystallized grains [22-24] and the impeding effect of high dislocation density at large strains [22,25]. In the early transformation stage, the volume fractions of the HCP-martensite and twins were relatively low. However, the thicknesses of such lamellar structures were very thin (<100 nm), thus reducing the mean free path of dislocations. The FCC fraction of the P750C-3m is \sim 58.5% at the true strain of \sim 26%, which is lower than that of the P750C-1m (\sim 64.4%) at the fracture point. More HCP martensite was formed in the P750C-3m than in P750C-1m during deformation, and then the HCP phase tends to share more load, enabling more plastic deformation in the FCC phase, which could contribute to the higher ductility in the P750C-3m.

Fig. 4(a) shows the deformed microstructure of the P750C-1m sample near the fracture surface by correlative EBSD and ECCI analyses. Note that the image acquisition plane is perpendicular to the LD. The IPF and phase maps reveal the martensitic transformation from the FCC to the HCP phase (~ 35% in area fraction) in both coarse parent grains and fine recrystallized grains upon tensile loading. The recrystallized region shows a higher KAM value than the parent grains, indicating a larger strain accommodation by the recrystallized grains. To further clarify the orientation dependence of the deformation mechanism, we selected grains with different orientations from the IPF map for ECCI analyses. For the grain with (001) orientation, 001_{FCC} in ROI I, a high density of dislocation cells is observed inside the cell blocks. In contrast, the 111_{FCC} grain (ROI II) is dominated by profuse deformation twins and HCP lamellae. Small deformation occurs in the 311_{FCC} grain (region III) due to a large number of pre-existing twins and shear bands in the matrix, Fig. 1(d), which correlates with the linear increase in the {311} lattice strain throughout the whole tensile stages, Fig. 2(b). Compared to the P750-1m sample, the P750-3m sample shows a larger area fraction of HCP phase (~ 53%) upon deformation, which even engulfs the entire FCC grains, in Fig. 4(b). The lower KAM value inside the HCP phase suggests less strain accommodation than the FCC phase. Close inspection of 001_{FCC} and 111_{FCC} grains (ROI I and II) shows similar deformation behavior to that of the P750-1m sample. However, the deformation twins and HCP lamellae are also activated in the 311_{FCC} recrystallized grain, which agrees well with the bending up of the {311} lattice strain

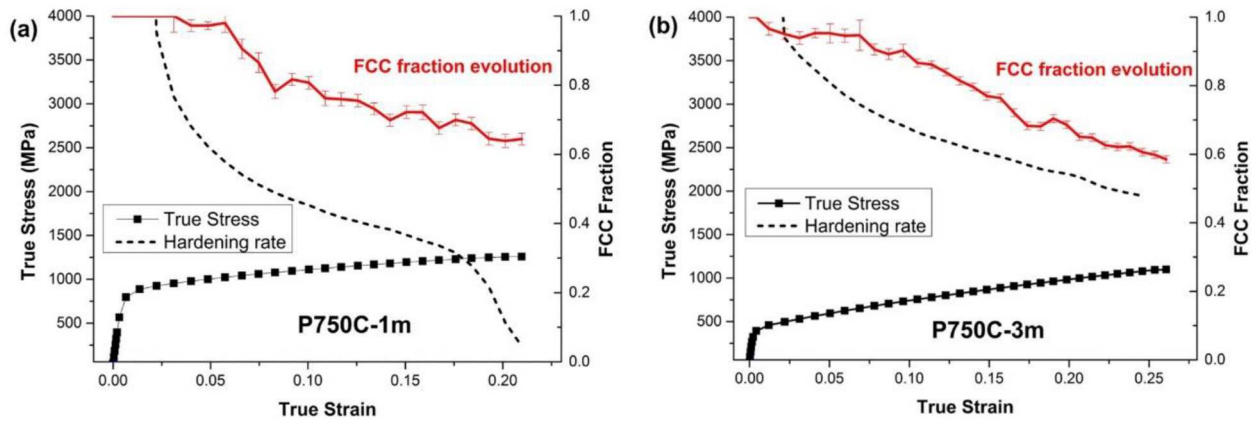


Fig. 3. FCC fraction evolutions with the corresponding true stress-strain curves and work hardening curves: (a) P750C-1m, (b) P750C-3m.

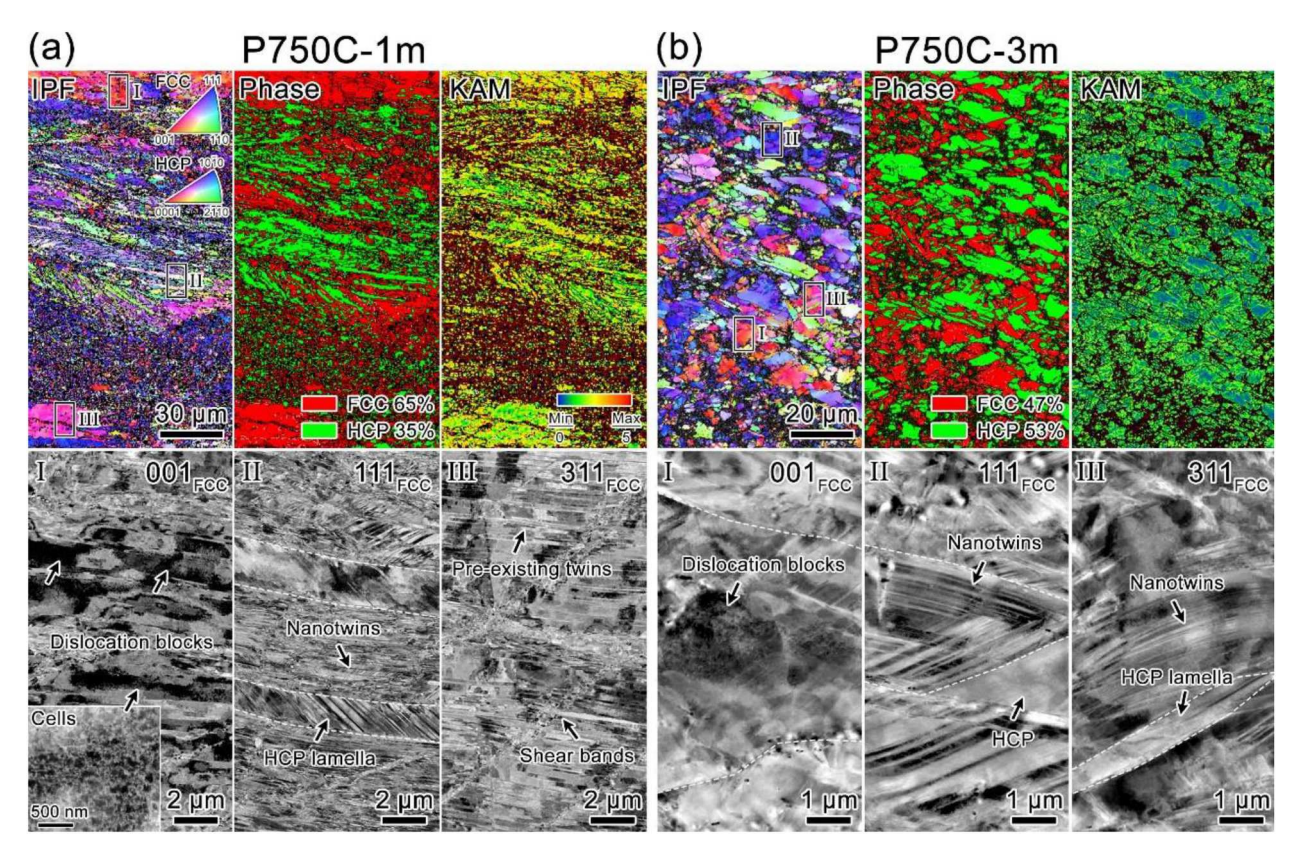


Fig. 4. EBSD IPF, phase, and KAM maps, and correlative enlarged ECC images of different grain orientations in the IPF maps obtained from (a) P750C-1m and (b) P750C-3m samples near the fracture surface.

along with the onset of HCP martensitic transformation, Fig. 2(d). As shown in the Fig. S1 in supplementary, the $\{111\}$ grain orientation preferred deformation texture was developed during plastic deformation, which could be resulting from the deformation twinning and FCC

to HCP phase transformation.

Fig. 5 shows the tensile properties, i.e., tensile strength vs. elongation, of the studied metastable HEAs comparing those with the traditional metallic materials [7,26-29] with the schematics of deformation

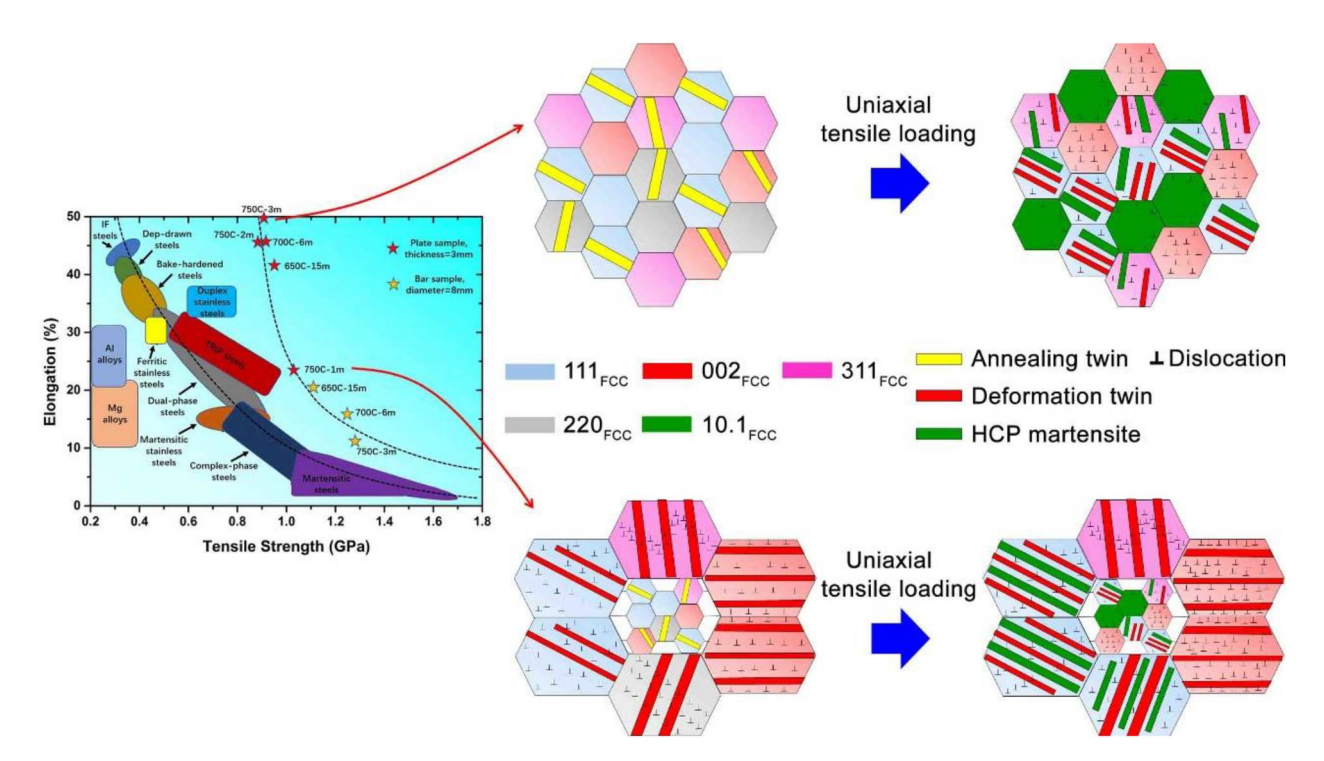


Fig. 5. The tensile properties (tensile strength vs. elongation) of the studied interstitial metastable HEAs in comparison with the traditional metallic materials, and corresponding schematics of deformation mechanisms in the alloys with different tensile properties.

mechanisms. A wide range of strength-ductility property was achieved using different thermal treatments in this metastable Fe_{49.5}Mn₃₀₋ Co₁₀Cr₁₀C_{0.5} HEA. This study used in-situ neutron diffraction, EBSD, and ECCI analyses to reveal the deformation mechanisms of the studied alloys, as shown in the schematics. For the sample with low strength and high ductility, a fully recrystallized microstructure leads to the low critical stress for activation of FCC to HCP transformation, Fig. 1(e) and 2(c-f). Given the low dislocation density and medium grain size [12,21, 30], the martensitic transformation and deformation twinning occur easily in both {111} and {311} FCC grain families, as shown by the vertical trend of lattice strain evolution in the early deformation stage, Fig. 4(b). The {002} grain family is dominant by dislocation slip due to the higher Schmid factor than that of the twinning systems [24,31]. In contrast, the samples with moderate strength and ductility had partially recrystallized microstructure before the deformation, Fig. 1(d). Because the pre-existing deformation substructures, i.e., dislocations and nano-twins, and grain refinement, can enhance the mechanical stability of FCC matrix [32,33], the HCP martensite is activated at a medium stress range and inhibited in the {111} grain family, Fig. 4(a). The {311} grains show little strain accommodation due to dense shear bands in the matrix, resulting in a linear trend of lattice strain upon deformation, Fig. 2(b-f). For the alloys with high strength and low ductility, deformed microstructure with intense dislocations, twins, and shear bands causes large stress to activate the martensitic transformation, Fig. 1(c) and 2

In summary, the continuous deformation mechanisms of interstitial metastable HEAs with different tensile properties are revealed in a complete picture via real-time in-situ neutron diffraction, EBSD, and ECCI analyses. A wide range of strength-ductility tradeoffs was obtained through a series of annealing procedures with generation of different initial microstructures in the $\rm Fe_{49.5}Mn_{30}Co_{10}Cr_{10}C_{0.5}$ alloy. The multistage work hardening behavior induced by FCC to HCP transformation could lead to a wide range of properties. The critical condition for such ideal cases could be tuned by different preparation processes, which could result in different deformation mechanisms by changing the load partitioning between FCC matrix and HCP martensite. This research provides a micromechanical origin of the above scenarios through the indispensable neutron diffraction measurements, due to reduced critical stress in the recrystallized grains and the activation of multiple slip systems.

Declaration of Competing Interest

The authors declare that they have no known competing financial interests or personal relationships that could have appeared to influence the work reported in this paper.

Data Availability

Research data in this work are available by sending direct requests to the corresponding author.

Acknowledgments

ZL, PKL, and YG are grateful for the support from the US National Science Foundation (DMR 1809640). ZL also acknowledges a graduate fellowship from the Center for Materials Processing at the University of Tennessee. Neutron diffraction work was carried out at the Spallation Neutron Source (SNS), which is the U.S. Department of Energy (DOE) user facility at the Oak Ridge National Laboratory, sponsored by the Scientific User Facilities Division, Office of Basic Energy Sciences.

Supplementary materials

Supplementary material associated with this article can be found, in the online version, at doi:10.1016/j.scriptamat.2023.115439.

References

- B. Cantor, I.T.H. Chang, P. Knight, A.J.B. Vincent, Microstructural development in equiatomic multicomponent alloys, Materials Science and Engineering A (2004) 213–218, 375-377.
- [2] J.W. Yeh, S.K. Chen, S.J. Lin, J.Y. Gan, T.S. Chin, T.T. Shun, C.H. Tsau, S.Y. Chang, Nanostructured high-entropy alloys with multiple principal elements: Novel alloy design concepts and outcomes, Advanced Engineering Materials 6 (2004) 299–303.
- [3] Y. Zhang, T.T. Zuo, Z. Tang, M.C. Gao, K.A. Dahmen, P.K. Liaw, Z.P. Lu, Microstructures and properties of high-entropy alloys, Progress in Materials Science 61 (2014) 1–93.
- [4] W. Li, D. Xie, D. Li, Y. Zhang, Y. Gao, P.K. Liaw, Mechanical behavior of highentropy alloys, Progress in Materials Science 118 (2021), 100777.
- [5] T. Yang, Y.L. Zhao, Y. Tong, Z.B. Jiao, J. Wei, J.X. Cai, X.D. Han, D. Chen, A. Hu, J. J. Kai, K. Lu, Y. Liu, C.T. Liu, Multicomponent intermetallic nanoparticles and superb mechanical behaviors of complex alloys, Science 362 (2018) 933–937.
- [6] Q. Pan, L. Zhang, R. Feng, Q. Lu, K. An, A.C. Chuang, J.D. Poplawsky, P.K. Liaw, L. Lu, Gradient cell–structured high-entropy alloy with exceptional strength and ductility, Science 374 (2021) 984–989.
- [7] P. Shi, R. Li, Y. Li, Y. Wen, Y. Zhong, W. Ren, Z. Shen, T. Zheng, J. Peng, X. Liang, P. Hu, N. Min, Y. Zhang, Y. Ren, P.K. Liaw, D. Raabe, Y.D. Wang, Hierarchical crack buffering triples ductility in eutectic herringbone high-entropy alloys, Science 373 (2021) 912–918.
- [8] Z. Li, K.G. Pradeep, Y. Deng, D. Raabe, C.C. Tasan, Metastable high-entropy dualphase alloys overcome the strength-ductility trade-off, Nature 534 (2016) 227–230.
- [9] Z. Lei, X. Liu, Y. Wu, H. Wang, S. Jiang, S. Wang, X. Hui, Y. Wu, B. Gault, P. Kontis, D. Raabe, L. Gu, Q. Zhang, H. Chen, H. Wang, J. Liu, K. An, Q. Zeng, T.G. Nieh, Z. Lu, Enhanced strength and ductility in a high-entropy alloy via ordered oxygen complexes, Nature 563 (2018) 546–550.
- [10] X. Li, Z. Li, Z. Wu, S. Zhao, W. Zhang, H. Bei, Y.F. Gao, Strengthening in Al-, Mo- or Ti-doped CoCrFeNi high entropy alloys: a parallel comparison, Journal of Materials Science & Technology 94 (2021) 264–274.
- [11] Y. Chen, J. Qiao, H. Diao, T. Yang, J. Poplawsky, W. Li, F. Meng, Y. Tong, L. Jiang, P.K. Liaw, Y.F. Gao, Extraordinary creep resistance in a non-equiatomic highentropy alloy from the optimum solid-solution strengthening and stress-assisted precipitation process, Acta Materialia 244 (2023), 118600.
- [12] J. Su, D. Raabe, Z. Li, Hierarchical microstructure design to tune the mechanical behavior of an interstitial TRIP-TWIP high-entropy alloy, Acta Materialia 163 (2019) 40–54.
- [13] J. Su, X. Wu, D. Raabe, Z. Li, Deformation-driven bidirectional transformation promotes bulk nanostructure formation in a metastable interstitial high entropy alloy, Acta Materialia 167 (2019) 23–39.
- [14] X.L. Wang, T.M. Holden, G.Q. Rennich, A.D. Stoica, P.K. Liaw, H. Choo, C. R. Hubbard, VULCAN—The engineering diffractometer at the SNS, Physica B: Condensed Matter (2006) 673–675, 385-386.
- [15] K. An, H.D. Skorpenske, A.D. Stoica, D. Ma, X.-L. Wang, E. Cakmak, First In Situ Lattice Strains Measurements Under Load at VULCAN, Metallurgical and Materials Transactions A 42 (2010) 95–99.
- [16] K. An, VDRIVE-Data reduction and interactive visualization software for event mode neutron diffraction, ORNL Report, Oak Ridge National Laboratory (2012). ORNL-TM-2012-621.
- [17] I. Gutierrez-Urrutia, D. Raabe, Dislocation and twin substructure evolution during strain hardening of an Fe-22wt.% Mn-0.6wt.% C TWIP steel observed by electron channeling contrast imaging, Acta Materialia 59 (2011) 6449-6462.
- [18] S. Fu, H. Bei, Y. Chen, T.K. Liu, D. Yu, K. An, Deformation mechanisms and work-hardening behavior of transformation-induced plasticity high entropy alloys by in-situ neutron diffraction, Materials Research Letters 6 (2018) 620–626.
- [19] Z. Li, C.C. Tasan, H. Springer, B. Gault, D. Raabe, Interstitial atoms enable joint twinning and transformation induced plasticity in strong and ductile high-entropy alloys, Scientific reports 7 (2017) 40704.
- [20] M. Wang, Z. Li, D. Raabe, In-situ SEM observation of phase transformation and twinning mechanisms in an interstitial high-entropy alloy, Acta Materialia 147 (2018) 236–246.
- [21] C.-S. Yoo, Y.-M. Park, Y.-S. Jung, Y.-K. Lee, Effect of grain size on transformationinduced plasticity in an ultrafine-grained metastable austenitic steel, Scripta Materialia 59 (2008) 71–74.
- [22] S. Mahajan, M.L. Green, D. Brasen, A model for the FCC→HCP transformation, its applications, and experimental evidence, Metallurgical Transactions A 8 (1977) 283, 293
- [23] S.L. Wong, M. Madivala, U. Prahl, F. Roters, D. Raabe, A crystal plasticity model for twinning- and transformation-induced plasticity, Acta Materialia 118 (2016) 140–151
- [24] I. Gutierrez-Urrutia, S. Zaefferer, D. Raabe, The effect of grain size and grain orientation on deformation twinning in a Fe-22wt.% Mn-0.6wt.% C TWIP steel, Materials Science and Engineering: A 527 (15) (2010) 3552-3560.
- [25] Y. Liu, H. Yang, G. Tan, S. Miyazaki, B. Jiang, Y. Liu, Stress-induced FCC

 martensitic transformation in CoNi, Journal of Alloys and Compounds 368 (2004)
 157–163.
- [26] P. Shi, W. Ren, T. Zheng, Z. Ren, X. Hou, J. Peng, P. Hu, Y.F. Gao, Y. Zhong, P. K. Liaw, Enhanced strength-ductility synergy in ultrafine-grained eutectic highentropy alloys by inheriting microstructural lamellae, Nature Communications 10 (2019) 489.
- [27] S. Rajasekhara, L. Karjalainen, A. Kyröläinen, P. Ferreira, Development of stainless steels with superior mechanical properties: a correlation between structure and

- properties in nanoscale/sub-micron grained austenitic stainless steel, Advanced Steels, Springer, 2011, pp. 371–384.
- [28] G. Welsch, R. Boyer, E. Collings, Materials properties handbook: titanium alloys, ASM international, 1993.
- [29] H. Huang, Y. Wu, J. He, H. Wang, X. Liu, K. An, W. Wu, Z. Lu, Phase-transformation ductilization of brittle high-entropy alloys via metastability engineering, Advanced Materials 29 (2017), 1701678.
- [30] K.M. Rahman, V.A. Vorontsov, D. Dye, The effect of grain size on the twin initiation stress in a TWIP steel, Acta Materialia 89 (2015) 247–257.
- [31] Y. Deng, C.C. Tasan, K.G. Pradeep, H. Springer, A. Kostka, D. Raabe, Design of a twinning-induced plasticity high entropy alloy, Acta Materialia 94 (2015) 124–133.
- [32] Y.-S. Jung, Y.-K. Lee, Effect of pre-deformation on the tensile properties of a metastable austenitic steel, Scripta Materialia 59 (2008) 47–50.
- [33] K. Sipos, L. Remy, A. Pineau, Influence of austenite predeformation on mechanical properties and strain-induced martensitic transformations of a high manganese steel, Metallurgical and Materials Transactions A 7 (1976) 857–864.